Physics of active jamming during collective cellular motion in a monolayer

Simon Garcia[a,b], Edouard Hannezo[a,c], Jens Elgeti[d], Jean-François Joanny[a], Pascal Silberzan[a,b,1], and Nir S. Gov[e,1]

[a]Laboratoire PhysicoChimie Curie, Institut Curie, Paris Sciences et Lettres Research University - Sorbonne Universités, Université Pierre et Marie Curie - Centre National de la recherche Scientifique, 75005 Paris, France; [b]Equipe "Biology-inspired physics at mesoscales" labellisée Ligue Contre le Cancer, Institut Curie, 75248 Paris, France; [c]Cavendish Laboratory, University of Cambridge, CB3 0HE Cambridge, United Kingdom; [d]Theoretical Soft Matter and Biophysics, Institute of Complex Systems and Institute for Advanced Simulation, Forschungszentrum Jülich, D-52425 Jülich, Germany; and [e]Department of Chemical Physics, Weizmann Institute of Science, Rehovot 76100, Israel

Edited by David A. Weitz, Harvard University, Cambridge, MA, and approved November 3, 2015 (received for review June 4, 2015)

Although collective cell motion plays an important role, for example during wound healing, embryogenesis, or cancer progression, the fundamental rules governing this motion are still not well understood, in particular at high cell density. We study here the motion of human bronchial epithelial cells within a monolayer, over long times. We observe that, as the monolayer ages, the cells slow down monotonously, while the velocity correlation length first increases as the cells slow down but eventually decreases at the slowest motions. By comparing experiments, analytic model, and detailed particle-based simulations, we shed light on this biological amorphous solidification process, demonstrating that the observed dynamics can be explained as a consequence of the combined maturation and strengthening of cell–cell and cell–substrate adhesions. Surprisingly, the increase of cell surface density due to proliferation is only secondary in this process. This analysis is confirmed with two other cell types. The very general relations between the mean cell velocity and velocity correlation lengths, which apply for aggregates of self-propelled particles, as well as motile cells, can possibly be used to discriminate between various parameter changes in vivo, from noninvasive microscopy data.

collective cell migration | jamming | glass transition | dynamic inhomogeneity | cell–cell adhesion

Collective motion of cells is crucial in many biological phenomena, including embryonic development (1), wound healing (2, 3), tissue repair (1, 4), and cancer (1, 4). Therefore, understanding the physics underlying how individually migrating cells combine their motion to collectively migrate is presently a matter of intense study. In this context, several studies have recently shown, by numerical simulations, that local alignment rules can result in the emergence of strongly correlated cellular motions in a confluent monolayer (5–9).

As time passes, these cell movements in the monolayer slow down. This classic observation is usually associated with the so-called "density-mediated contact inhibition of locomotion" (10, 11). To go further in the analysis of this phenomenon, several observations (6, 12, 13) and simulations (7, 14, 15) give an interesting new angle by emphasizing the analogy between a cell monolayer and a bidimensional "jammed" colloidal system, where the individual motions of the particles are confined in "cages" of the size of the particles, and where the whole system behaves as a solid (16–19). In particular, the increase in the characteristic length scales describing the velocity field as well as the presence of "giant" density fluctuations (20, 21) appear to validate this analogy. As a consequence, several theoretical descriptions have been proposed for these cell assemblies within the conceptual framework used to describe jamming in active systems (6, 12, 13, 22–24).

Cellular density (the equivalent of the packing fraction in colloidal systems) is often assumed to be the principal control parameter in these systems (6, 12, 25–27). However, because cellular densities vary between cell types and growing conditions, other parameters such as (*i*) cell–cell adhesion energy, (*ii*) magnitude of cellular forces and persistence time for these forces (28), or (*iii*) cell shape (15) have also been considered. Any of these parameters could a priori contribute to the jamming transition, and discriminating between each contribution is not possible at present.

In the present study, we investigate the motion of a proliferating, motile, population of immortalized human bronchial epithelial cells (HBEC) (29). Even though cellular density increases during the time course of our experiments, we find that it is not the main control parameter to describe the collective motion of these cells. Rather, we observe that the decrease in cell motility is due to the maturation of cell–cell and cell–substrate junctions. We find that the HBEC cellular monolayer changes from a fluid-like regime of fast motion at early times to an amorphous solid-like ("glassy") regime at late times, and this transition is mainly driven by changes in the cell–cell adhesion and friction. This transition can be formalized in a simple analytical model and in numerical simulations that both describe well our experimental observations. We furthermore demonstrate that the same framework describes cells that do not develop cell–cell adhesions (NIH 3T3 fibroblasts), as well as strongly adherent epithelial cells [Madin Darby Canine Kidney (MDCK)]. We thereby identify a cellular mechanism where the path to glassiness is dominated by increasing the effective interaction potentials, rather than density (18, 22).

Results

Cellular Slowing Down and Evolution of the Velocity Correlations. We have experimentally studied the dynamics of immortalized HBEC cells in a monolayer and its evolution over time. For these

Significance

Collective cell motion is very important in many biological processes such as wound healing, embryogenesis, or cancer progression. Nevertheless, it is not clear which parameters control the transition from freely moving single cells to collective jammed motion. In this article, we uncover complex dynamics as a cell monolayer ages, where cell motion is shown to gradually slow down with time, while the distance over which cell displacements are correlated first increases drastically and then decreases. This change of behavior is not controlled by cell density but rather by a maturation of the cell–cell and cell–substrate contacts. By comparing experiments, analytic model, and detailed particle-based simulations, we shed light on this biological amorphous solidification process.

Author contributions: P.S. and N.S.G. designed research; S.G., E.H., J.E., P.S., and N.S.G. performed research; J.-F.J., P.S., and N.S.G. contributed new reagents/analytic tools; S.G., E.H., J.E., P.S., and N.S.G. analyzed data; and S.G., E.H., J.E., P.S., and N.S.G. wrote the paper.

The authors declare no conflict of interest.

This article is a PNAS Direct Submission.

Freely available online through the PNAS open access option.

[1]To whom correspondence may be addressed. Email: nir.gov@weizmann.ac.il or pascal.silberzan@curie.fr.

This article contains supporting information online at www.pnas.org/lookup/suppl/doi:10.1073/pnas.1510973112/-/DCSupplemental.

weakly cohesive cells, confluence could not be accurately defined because, at low density, the cells were very dynamic, the population being best described as a cellular gas with low interactions between particles. This state was followed by a situation where the cells remained very motile but with no more voids between them because of the larger cell density ("fluid phase"), at which point the velocity gradually decreased. This system therefore exhibits fast keratinocyte-like motion at early times and epithelium-like motion at late times. Of note is that, by analyzing the density fluctuations in the layer, we found the characteristic signature of nonequilibrium dynamics, namely giant number fluctuations (30) (Fig. S1).

By mapping the displacement field within the monolayer over time (3) (Movie S1 and Fig. 1*A*), we first measured the overall cell speed, or root-mean-square (rms) velocity v_{rms}, in the layer and observed that it decreased monotonously (Fig. 1*B*) with time until it became too small to measure. We then computed the velocity–velocity spatial correlation function $C_{vv}(r)$ for each time, from which we extracted a correlation length $\xi_{vv}(t)$ (Fig. 1*C*; see details in *Materials and Methods*). This correlation length was small (of order two to three cell sizes) at the beginning of the experiment (Fig. 1*D*), and then increased to a value corresponding to approximately seven cell sizes over the course of several hours. Eventually, at later times, ξ_{vv} decreased again to the single cell size. Fig. 1*C*, *Inset*, demonstrates that a single exponential decay allowed us to extract ξ_{vv} throughout the whole process of cellular slowing down.

Inspired by previous work (6, 12, 26), we first tried to correlate this progressive slowing down of the cells with their surface density ρ. Indeed, because of proliferation, ρ did increase over time. However, the relation $v_{rms} \approx 1/\sqrt{\rho}$ (25, 27) that has been previously found in another cell type was not consistent with the slowdown of the cells that we observed at long times, suggesting that it was not dominated by the increase in density. Furthermore, we noticed that, in the present case, the velocity decreased by a factor of 10 and the density increased only by a factor of 2 (from 1.5×10^5 cells per square centimeter to 3.2×10^5 cells per square centimeter) in the time course of our experiments (Fig. 1*B*) (compared with factors of 2 and 3, respectively, in ref. 27). Finally, because it was practically not possible to dynamically access the cell density from the phase contrast images in dense monolayers, we reasoned that, if density was the major control parameter, it is expected that different experiments performed with different initial seeding density would be described by the same $\xi_{vv}(t)$ curve with a shift in times. This is not, however, what was observed (Fig. 2*A*). Furthermore, at a given time and for the same number of cells seeded on the substrate, $\xi_{vv}(t)$ and ρ were found to be uncorrelated (Fig. 2*B*). (The absolute value of Pearson's coefficient measured at different times over eight FOVs was smaller than 0.3.) Altogether, these observations point to an aging process of the monolayer distinct from a simple increase in density. By aging, we mean here that the cellular monolayer changes its dynamical properties with time, associated with the maturation of cell–cell and cell–substrate contacts.

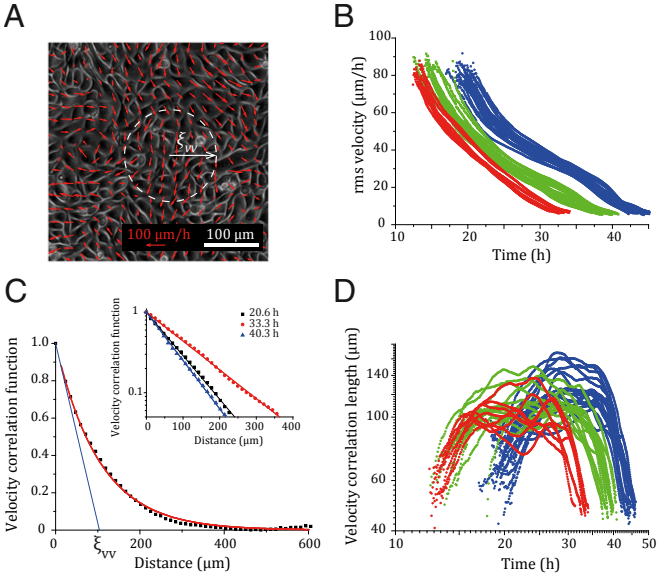

Fig. 1. Dynamics of the HBEC tissue. (*A*) Example of a velocity field obtained through PIV superimposed on the corresponding phase contrast image of the monolayer. (*B*) Evolution of rms velocity v_{rms} in the tissue with time. Blue, green, and red curves correspond to different initial number of cells seeded in the well around 640,000, 960,000 and 1,280,000 cells, respectively. (*C*) Velocity–velocity radial correlation function $C_{vv}(r)$. Fitting a decreasing exponential function gives the correlation length ξ_{vv}. (*Inset*) Radial correlation function $\xi_{vv}(r, t)$ in semilog scale, at three different time points for a representative field of view (FOV) picked among the wells seeded with 640,000 cells. The solid lines are the decreasing exponential functions fitted to the data points. Black, t = 20.6 h and ξ_{vv}= 79 μm; red, t = 33.3 h and ξ_{vv}= 122 μm; blue, t = 40.3 h and ξ_{vv}= 73 μm. (*D*) Evolution of ξ_{vv} with time after seeding for 39 FOVs (color code is the same as in *B*).

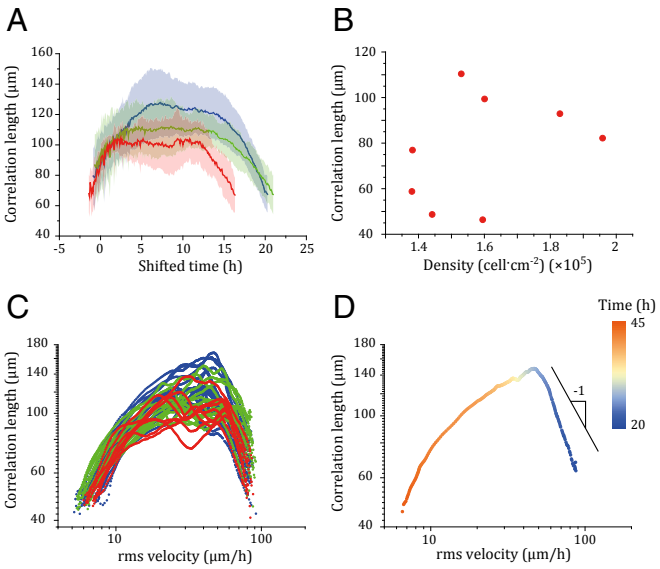

Fig. 2. Velocity controls the correlation. (*A*) Comparison of the $\xi_{vv}(t)$ evolution curves for different seeding densities. The times have been shifted to superimpose the early evolutions. (*B*) No significant correlation between ξ_{vv} and cell density ρ_{cell} was found for given time points. Here, eight FOVs were picked among the wells seeded with 640,000 cells at t = 21 h. Pearson's correlation coefficient is r = 0.34. (*C*) The different $\xi_{vv}(v_{rms})$ curves (same data as Fig. 1*D*) nicely superimpose and describe a single master curve. (*D*) Evolution of the monolayer in the v_{rms}–ξ_{vv} space for a representative FOV.

Analysis in Terms of Effective Clusters. Motivated by these unexpected observations, we first analyzed the cellular layer in terms of fictitious clusters, which are defined to have the radius of the velocity–velocity correlation length ξ_{vv}. Each such cluster is assumed to move as a solid object, so that all of the cells inside it have the same velocity, and are therefore perfectly correlated in their motion. This amounts to replacing the exponential decay in the velocity correlations by a step function at radius ξ_{vv}.

We characterize the random active (motile) forces induced by the individual cells as having a typical force f_0 and a mean burst length τ_{noise} (persistence time of the cellular traction force). We then solve the Langevin equation for the center-of-mass motion of a cluster (31) to access the average cluster speed, v_{rms}, in the limit of vanishing inertial effects $\lambda\tau_{noise} \gg 1$, where λ is the effective friction coefficient of the cluster. In these active systems, v_{rms} can be viewed as representing the effective temperature. We

consider the two extreme cases of no correlation or perfect correlation between the individual traction forces of the cells inside the cluster. We therefore get

$$\langle v^2\rangle_{nocor} = \frac{Nf_0^2}{2\lambda^2},\ \langle v^2\rangle_{cor} = \frac{N^2 f_0^2}{2\lambda^2} \quad [1]$$

where N is the number of cells in the clusters ($N \propto \xi_{vv}^2$).

If the friction is dominated by the cell–substrate interactions, we have $\lambda \propto \xi_{vv}^2$, and we get from Eq. **1** that (Fig. S2)

$$\langle v^2\rangle_{nocor} \propto \frac{1}{\xi_{vv}^2} \Rightarrow \sqrt{\langle v^2\rangle_{nocor}} = v_{rms} \propto \frac{1}{\xi_{vv}},\ \langle v^2\rangle_{cor} \propto \xi_{vv}^0. \quad [2]$$

For a partially correlated cluster, we therefore expect $\xi_{vv} \propto v_{rms}^{\alpha}$, where $\alpha < -1$.

Another interesting limit is the situation where effective friction is dominated by cell–cell interactions rather than cell–substrate interactions. Then, most of the dissipation takes place at the perimeter of the clusters and, therefore, $\lambda \propto \xi_{vv}$. Using this relation in Eq. **1**, we get (Fig. S2)

$$\langle v^2\rangle_{nocor} \propto \xi_{vv}^0,\ \langle v^2\rangle_{cor} \propto \xi_{vv}^2 \Rightarrow \sqrt{\langle v^2\rangle_{cor}} = v_{rms} \propto \xi_{vv}. \quad [3]$$

We find that, for motion dominated by cell–cell friction, the rms velocity v_{rms} increases with the correlation length ξ_{vv} (Eq. **3**). It is highly plausible that, when cell–cell interactions (effective friction) are strong, the cellular traction forces become highly correlated. In that case, our model predicts (according to Eq. **3**) that $\xi_{vv} \propto v_{rms}$.

Motivated by this cluster analysis, we plotted the velocity correlation length as a function of the v_{rms} of the cells (Fig. 2 *C* and *D*). All experiments (including different seeding densities) collapsed onto a characteristic universal bell-shaped curve (Fig. 2*C*) for different experiments, suggesting that v_{rms} is indeed the correct control parameter. For large velocities, we find that the power-law relations (Eqs. **2**) that predict an exponent −1 in the case of uncorrelated noise seem to describe the data reasonably well (Fig. 2*D*), which would indicate that, in this regime, the effective friction is dominated by cell–surface interactions (as in ref. 31).

In contrast, at low velocities, the slope became positive, with the correlation length decreasing with further slowing down (bell-shaped curve in Fig. 2 *C* and *D*). The presence of such a second regime was highly surprising. Altogether, these data and analysis suggest that the layer is initially (high-speed regime) fluid-like with low coherence in the motile forces that neighboring cells exert, and is dominated by constant cell–surface effective friction. At later times (low speeds), the behavior changes, which may indicate that cell–cell (and cell–substrate; Fig. 3) interactions could dominate the internal friction and also give rise to correlated traction forces. Note that the density evolution is only secondary in this interpretation, in contrast with other systems (32).

What could then be the mechanism driving this change in behavior of the cellular layer? Our simple clusters model hints at increased cell–cell interactions, so we sought to verify this prediction by looking for changes in the cadherin intensity at the cell–cell junctions. As shown in Fig. 3 *A* and *B*, we found that, as the cell layer ages, the cadherin concentration at the cell–cell junctions normalized by cytoplasmic cadherin concentrations, significantly increased between day 1 and day 3. This is in agreement with a similar behavior found previously in small cellular islands (33), where the increase of cell–cell adhesion with culture age decreased the expansion velocity of the cells. We also found that cell–substrate adhesion, labeled by vinculin, which is a member of the focal adhesion (FA) complex (34, 35), became more homogeneously spread over the entire cell–substrate surface with time (Fig. 3*C*). The well-defined FAs that were initially present disappeared progressively between day 1 and day 3. From these observations, we can therefore conclude that, as time goes, the system ages by maturation of cell–cell cadherin-mediated contacts and cell–substrate adhesions.

We now consider a more detailed model for cell–cell and cell–substrate effective friction. We model the effective friction as arising from transient molecular adhesions that undergo binding–unbinding dynamics, and that are affected by the shear forces. The molecular linkers are of the "slip bond" type, so that applied shear forces due to relative velocity between the cells, or between the cell and substrate, tend to detach them (Fig. S4). During the times that these linkers are attached, and stretched by the relative velocity, they exert a restoring force as they are assumed to behave as simple Hookean springs. This restoring force acts to resist the motion and therefore gives rise to an effective friction term. The strength of the friction coefficient due to these linkers depends on the number of attached linker (adhesion) molecules, and therefore increases sharply when the velocity is reduced and their detachment rate decreases. Details of the calculations are given in *Supporting Information*. The result is shown in Fig. 4 for uncorrelated motile cellular forces, and smoothly connects between the $v_{rms} \propto 1/\xi_{vv}$ behavior at large velocities and a turnover at lower velocities. There is good qualitative agreement between this theoretical result (Fig. 4 and Figs. S5 and S6) and the experimental observations (Fig. 2*C*). This suggests that the experimentally observed turnover in the v_{rms} vs. ξ_{vv} relation arises due to a continuous increase in the importance of cell–cell and cell–substrate frictions, through molecular adhesions, as the cellular layer slows down.

We tested the generality of the model with other cell types. MDCK cells develop very strong cell–cell adhesions, and NIH 3T3 fibroblasts remain highly motile and independent. These two cell types illustrate the limiting cases observed with the HBEC cells, with ξ_{vv} increasing with v_{rms} for MDCK and ξ_{vv} decreasing with v_{rms} for 3T3 cells (Fig. S7 *A* and *B*, respectively). The model therefore appears very general and is applicable to other cell types in the relevant regimes.

Theoretical Model of Interacting Active Particles: Different Routes to Slowing Down. The theoretical treatment presented so far in terms of effective clusters relates the mean cellular velocities (v_{rms}), that play the role of an effective temperature, to the velocity correlations length (ξ_{vv}) (Eqs. **1**–**3** and Eqs. **S1**–**S17**), and it

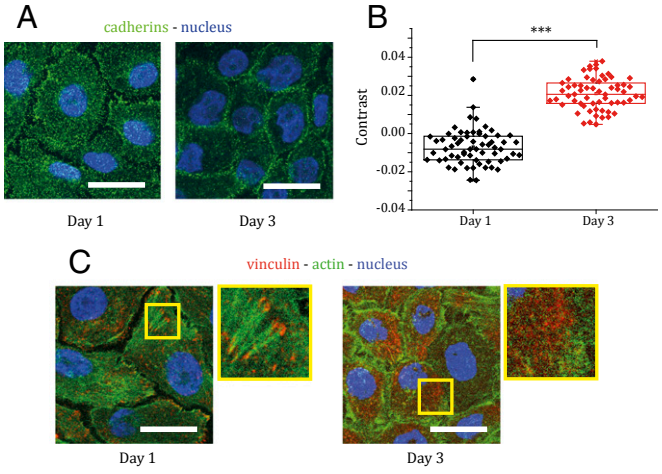

Fig. 3. Aging of the system through maturation of adhesion proteins with time. (*A*) Tissue stained for cell–cell junctions. Cadherin concentration is observed to increase at the cell–cell contacts as the cell layer ages. (*B*) Quantification of the contrast in cadherin signal between the junction and the cytoplasm. (*C*) As the layer ages, vinculin distribution is observed to evolve from small complexes at the ends of actin filaments to a more homogeneous and uniform distribution over the whole cell–substrate contact area. (Scale bars: 20 μm.)

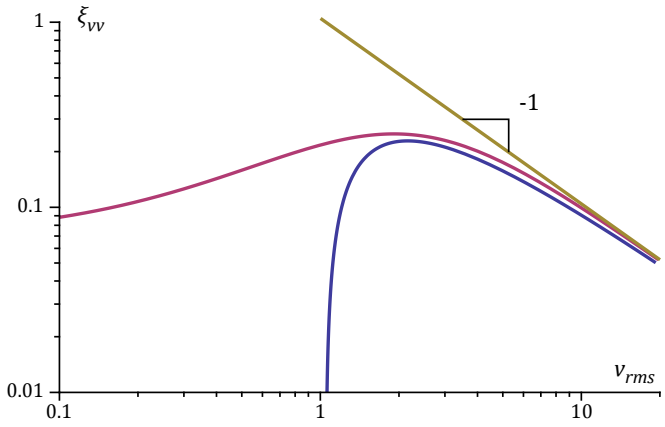

Fig. 4. Calculated v_{rms}–ξ_{vv} relation using the cluster analysis. Brown line, $v_{rms} \propto 1/\xi_{vv}$ relation for uncorrelated noise and constant friction (Eq. **2**); blue and purple lines, uncorrelated noise and velocity-dependent cell–cell and cell–substrate friction, respectively (Eqs. **S13** and **S17** and Figs. S5 and S6). At low velocities, the cell–cell or cell–substrate adhesion molecules are able to exert an increasingly effective friction due to their increasing lifetime. For cell–cell adhesion, we find that there is a minimal velocity at which the correlation length ξ_{vv} vanishes (Eqs. **S14**). For cell–substrate friction, the ξ_{vv} does not vanish at any velocity, but there is a pronounced maximum (Fig. S6).

suggests a possible underlying mechanism leading to cellular slowing down in the first place.

To validate these predictions theoretically, we resorted to particle-based simulations of self-propelled (active) interacting particles (based on ref. 9). In this simulation, we treated each particle as having a constant internal propulsive force, with a polarization vector that is diffusing freely in all directions. Each particle has the same properties, it is coupled to its neighbors through a short-range repulsive, medium-range attractive potential, and it experiences an additional velocity-dependent frictional force (both with the substrate and with neighboring cells). The details of the model and the fitting to the experimental data are given in *Supporting Information*. Note that this model was used without any explicit orientational interactions of the Vicsek type (5, 6, 8) in this system.

From the experiments (Fig. 3) and analysis (Figs. 2*C* and 4) described above, we have evidence that both cell–cell and cell–substrate adhesion evolve as the cell layer ages. However, there could, in principle, be several other changes in the cellular behavior that contribute to the effect of slowing down. The advantage of using simulations is that we can explore independently the different "routes" to slowing down, and compare them with the experiments. In addition to the effect of increase in the attractive interaction between the cells (described by the potential scaling factor k), we also consider the following effects: (*i*) decrease in the propulsion force f_0 produced by each particle, (*ii*) increase in the friction of the cells with the substrate λ_0, and (*iii*) increase in the cell–cell effective friction λ_{cell}. It is not a priori clear if all or any of these routes would give the experimentally observed relation between the velocity and correlation length.

In Fig. 5, we summarize the results of the simulations. Interestingly, we find that each of these routes gives rise to distinguishably different scaling behavior. Stronger cell–cell adhesive contacts should manifest in our model as stronger cell–cell potential (k). We find that, when this parameter of the model increases in magnitude, the slowing down follows a scaling $1/\xi^{\alpha}$, with $\alpha \cong 1$ (Fig. 5*A*). This is in agreement with the observed scaling in the experiments (Fig. 2*D*, fast regime). The route of decrease in the traction forces or increase in cell–cell effective friction produces a much shallower scaling $\alpha < 1$ (Fig. 5 *B* and *C*), whereas increasing cell–substrate friction gives a completely opposite correlation ($\alpha < 0$, Fig. 5*D*). The case of increasing particle density that does not seem to pertain to the experiments we present here (Fig. 2*B*) yields an exponent that strongly depends on the form of the interaction potential between the cells (Fig. 5*E*), and its slope is generally not in the observed range.

Specifically, for increasing cell–cell attractive potential (k), we find that the same $\xi_{vv} \propto v_{rms}^{\alpha}$ scaling relation is satisfied continuously from the fluid phase (low k) all of the way to the solid phase (high k) (Fig. 5*A*). Throughout, the velocity correlations decay with a single exponential, allowing us to extract ξ_{vv} (Fig. S8). The turnover in the observed v_{rms}–ξ_{vv} relation (Fig. 2 *C* and *D*) is therefore not directly due to the increasing strength of the cell–cell interaction potential alone. Following the analytic results of Fig. 4, we simulate a system whereby we increase the cell–cell adhesion strength, while the cell–substrate friction increases in a nonlinear manner for slow velocities (large k). This is done following the indications from the analytic model that introduces a velocity-dependent effective friction coefficient (Fig. 4), and due to the observation (Fig. 3*B*) that shows evolving cell–substrate adhesion (and effective friction) as the layer slows down. The result of such simulations is shown in Fig. 5*F*, which resembles very closely the observations (Fig. 2*C*) and the analytic calculation (Fig. 4, purple line). This behavior was found to be a robust feature of the simulations, independent of the particular choice of parameters (Fig. S9). Movies S2 and S3 visualize the dynamics in the fluid regime, and near the peak of the ξ_{vv} vs. v_{rms} curve (Fig. 5*F*), respectively.

To conclude, we find, from the above comparison between the experiments and the theory, that the observed peak in the ξ_{vv} vs. v_{rms} relation (Fig. 2 *C* and *D*) is not likely to arise from a liquid–solid

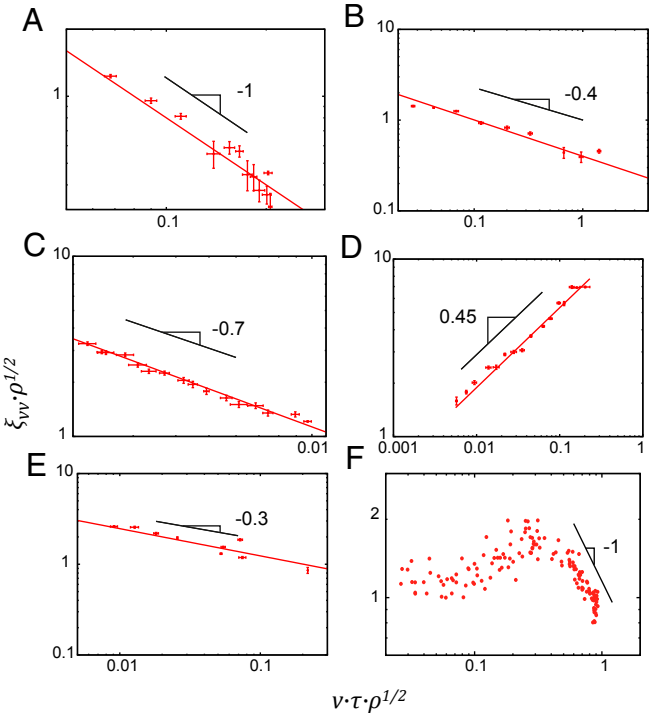

Fig. 5. Simulations of cellular dynamics. Simulated v_{rms}–ξ_{vv} relation while changing only one parameter in the model (symbols), while keeping the others fixed to the values specified in *Materials and Methods*: (*A*) increasing cell–cell adhesion (k), resulting in a power-law (solid line) $v_{rms} \propto 1/\xi_{vv}^{\alpha}$, with $\alpha = 1 \pm 0.03$; (*B*) decreasing cell propulsive force (f_0), resulting in $\alpha = 0.37 \pm 0.02$; (*C*) increasing cell–cell effective friction, resulting in $\alpha = 0.66 \pm 0.04$; (*D*) increasing cell–substrate friction, resulting in $\alpha = -0.45 \pm 03$; (*E*) increasing the cell density, resulting in $\alpha = -0.32 \pm 0.04$ (but strongly depends on the interaction strength); and (*F*) increasing cell–cell adhesion, while increasing nonlinearly the cell–substrate friction at low velocities, for $\lambda_0 = 1$. All graphs are plotted in rescaled units (see *Materials and Methods*).

transition but is due to an increase in the effective cell–cell and cell–substrate frictions, as cell–cell and cell–substrate adhesions mature with time (Fig. 3). Note that, because we are simulating a dense and constant density system, our results do not depend on the specific form of the effective interparticle potential. Note that use of an effective potential that acts between the cells (particles) is a coarse-grained simplification of the complex cell–cell interactions.

Dynamical Heterogeneities. The solidification process of disordered, glassy systems is often characterized by large dynamic heterogeneities (12, 23, 36–38). One way that the dynamic heterogeneities are quantified is by analyzing the mean size of clusters of the fastest 20% of particles in the system (12) (ξ_{het}), which we plot as a function of v_{rms} (Fig. 6*A*). We find that ξ_{het} does not scale with the velocities in the same way as ξ_{vv} (Fig. 2 *C* and *D*). Although ξ_{vv} changes by a factor of ∼3 over the course of the layer aging, the heterogeneity length scale ξ_{het} changes by a factor of ∼1.5 only. Compared to the simulations, this qualitative agreement is a further indication that, as the cellular layer slows down, it behaves as an amorphous, glassy solid. The inhomogeneous nature of the distribution of fast particles is shown in Fig. 6 *B* and *D* from the experiments and from simulations at the limits of cell–cell adhesion strength, respectively.

Conclusion

Let us summarize our main findings: We show that HBEC monolayers slow down over time, a process that is driven by the maturation of cell–cell (and cell–substrate) contacts. As the cellular monolayer slows down, we observe a change from a regime of fast-flowing cells that is dominated by a constant (i.e., velocity-independent) effective friction coefficient between the cells and the substrate to a regime of slow-moving cells that is dominated by a velocity-dependent effective friction coefficient. This transition in the system dynamics is driven by the increase in the effective friction coefficient when the relative velocity between the cells (and between the cells and the substrate) decreases.

At the slowest cell velocities, the motion within the monolayer is reduced to such low levels that, over the observation time, the cells hardly move beyond their own size. In this regime, the monolayer may be treated as an amorphous solid, for all practical purposes, and is therefore similar to the glass phase of nonliving amorphous matter. This similarity is demonstrated, for example, by the growth of dynamic heterogeneities shown in Fig. 6. We do not observe any sharp "phase transitions"; rather, the slowdown is a dynamic change in the dominant internal forces that control the motion. In this respect, the cellular system studied here exhibits a path to glassiness that is dominated by increasing the effective interparticle interaction potentials, rather than density, in the classical glass phase diagram (18, 22). This is somewhat similar to recent observations of jamming due to interplay between cell–cell interactions and cell shapes (39).

These conclusions are derived using experiments, simple analytic models, and detailed particle-based simulations, which allow us to dissect the underlying mechanisms even in a complex system such as collective cell motion. We have also demonstrated that the general mechanism and analysis developed here work well either for cells that do not develop cell–cell adhesions (fibroblasts NIH 3T3) or cells that form strong adhesions (MDCK epithelial cells). In both cases, we were able to recover specific regimes observed when using HBEC cells: MDCK show the increase of ξ_{vv} vs. v_{rms} expected for cells developing adhesions, whereas the 3T3 cells show the regime of a decrease of ξ_{vv} with v_{rms} expected for cells that do not develop cell–cell adhesions (Fig. S7 *A* and *B*). These two additional cell types show that the same theoretical framework can be applied to these very different situations.

Our study demonstrates that cellular layers behave as active, granular 2D matter. We find that velocity correlations arise due to the inherent persistence of the traction forces of the individual cells, even in the absence of explicit orientational interactions [such as of the Vicsek form (6, 7, 9)]. Comparing the simulations and the statistical data from the experiments, we are able to determine that the dominant mechanism responsible for the cellular slowing down is driven by an increase of cell–cell adhesion. Orientational interactions that align the traction forces of neighboring cells do exist but do not seem to have a strong effect in the present system. Other cellular systems may be more strongly dominated by such interactions (8). In fact, orientational ordering, similar to the changes in cell–substrate friction, produces a positive correlation between the cellular velocities and the velocity correlation length. Thus, we demonstrate that our framework allows us to conclusively discriminate between different types and classes of mechanisms that affect the collective dynamics in vitro. Therefore, it could, in principle, be directly applied to data acquired in in vivo situations.

Beyond cellular behavior, our work is relevant to the general study of active out-of-equilibrium systems. We obtain scaling relations between the velocity and the correlation length that dense active matter obeys, as it changes from a highly fluid to an amorphous (glass-like) solid.

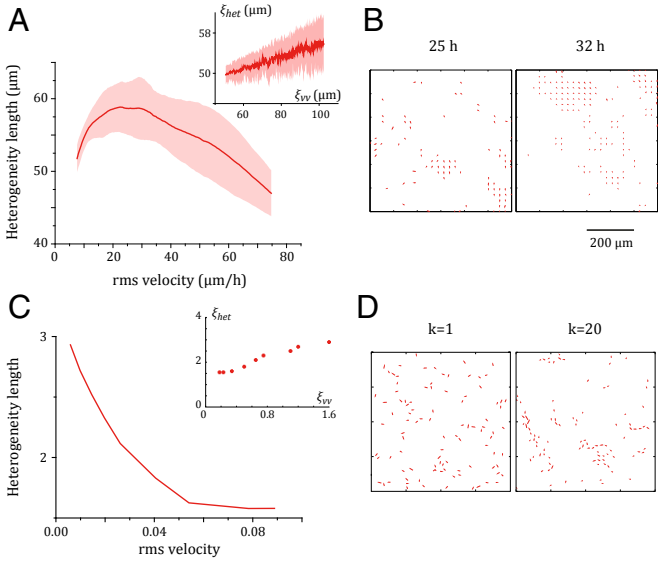

Fig. 6. Dynamics of fast clusters. (*A*) Evolution of the experimentally measured heterogeneity length ξ_{het} with the rms cell velocity v_{rms}. (*Inset*) Heterogeneity length plotted against the speed–speed correlation length, ξ_{het} vs. ξ_{vv}. (*B*) Inhomogeneous nature of the spatial distribution of the fast cells (red arrows) at different times in the experiments. (*C*) Same as *A* from the simulated data. Note that, because no increasing friction was implemented in this simulation, the curve decreases monotonously. In both the simulations and experiments, the heterogeneity length (ξ_{het}) varies much less than the velocity correlation length (ξ_{vv}) for the same velocity range. (*D*) Same as *B* from simulations, for a fluid-like ($k = 1$, *Left*), and solid-like ($k = 20$, *Right*) cell layer. Note that in both the simulations (*D*) and experiments (*B*), the fast cell are more dispersed in the high-velocity regime but form more compact clusters and streams in the low-velocity (v_{rms}) regime.

Materials and Methods

Detailed materials and methods can be found in *Supporting Information*.

Cell Culture and Seeding. We conducted experiments using immortalized (29) HBEC, a kind gift from J. Minna's laboratory in Dallas, TX. HBEC cells were grown in supplemented Keratinocyte serum-free medium. MDCK and NIH 3T3 cells were grown in supplemented DMEM. For videomicroscopy experiments, cells were seeded on polystyrene-bottomed 12-well tissue culture plates, keeping track of the seeding cell density.

Microscopy. Time-lapse multifield experiments were performed in phase contrast on an inverted microscope equipped with a 10× objective, at 37 °C under

5% CO_2 partial pressure and 95% relative humidity atmosphere. Fixed cells were observed in fluorescence at high magnification by confocal microscopy.

Immunocytochemistry and Fluorescence Staining. Cells were fixed with 4% (wt/vol) paraformaldehyde and immunostained for E-cadherin or vinculin. F-Actin and nuclei were respectively labeled with phalloidin and DAPI.

For density fluctuations measurements, living cells were stained with Hoechst 333422.

Velocity Fields. Most of the image processing was performed using MATLAB. Particle image velocimetry (PIV) analysis (40) was conducted using a custom algorithm based on the MatPIV software package for MATLAB (3, 41). For all purposes, the mean velocity $\langle\vec{v}\rangle$ was subtracted from calculated velocity fields $\vec{v}$ to avoid any drift-related bias and to get the fields: $\vec{v}^* = \vec{v} - \langle\vec{v}\rangle$. The details of the calculation of the velocity autocorrelation length $\xi_{vv}(t)$ from the correlation function are available in *Supporting Information*.

Fast Clusters and Heterogeneity Length. The fast clusters were determined at each time point by identifying the 20% of vectors with greatest modulus in our velocity field and then considering as clusters all of the contiguous regions (12). Heterogeneity length ξ_{het} was then calculated at each time point as the equivalent diameter of the average area of the fast clusters: $\xi_{het}(t) = \langle (4/\pi)\, A_{clust}(t)\rangle^{1/2}$.

Density Measurements. Cellular density ρ_{cell} in the time-lapse experiments was determined by manual pointing and clicking. For density fluctuations analysis with Hoechst-labeled cells, images were binarized and processed with Fiji (42), a distribution of open-source ImageJ software (43) focused on biological image analysis.

Simulation Model. Inspired by recent particle-based models for motile cells (9) (44), each motile cell is modeled as a soft sticky 2D circle, with a constant motility force of strength f_0, of mean persistence time τ. Each cell interacts with its neighbors through a soft short-range repulsion, medium-range attraction potential, with a potential stiffness k and equilibrium distance r_n. Dissipation occurs through a dampening of the radial component of the relative velocity between particles (45), and a background friction λ. The simulations presented are inherently unitless, and we present our simulation results without units. In *Supporting Information*, we provide explanations for the choice of parameter values in the simulations to match the experimental data.

ACKNOWLEDGMENTS. We thank Isabelle Bonnet, Axel Buguin, Jacques Camonis, Fanny Cayrac, Sylvie Coscoy, Guillaume Duclos, Philippe Marcq, Maria Carla Parrini, and the members of the "biology-inspired physics at mesoscales" group for discussion and advice. We acknowledge the Cell and Tissue Imaging Platform (member of France-Bioimaging) of the Genetics and Developmental Biology Department (UMR3215/U934) of Institut Curie and, in particular, Olivier Renaud and Olivier Leroy. The laboratoire PhysicoChimie Curie is part of the Labex CelTisPhyBio. E.H. acknowledges the Bettencourt-Schueller Foundation's Young Researcher Prize and Trinity College's Junior Researcher Fellowship for their support. N.S.G. and P.S. thank the Kavli Institute for Theoretical Physics (KITP) at Santa Barbara for its hospitality during the Workshop on Active Matter. This research was supported in part by the National Science Foundation under Grant NSF PHY1125915 for the workshop program at KITP. N.S.G. acknowledges the Institut Curie's Mayent-Rothschild Visiting Professor fund and Labex CelTisPhyBio for their support during the stay at the Institut Curie. N.S.G. is the incumbent of the Lee and William Abramowitz Professorial Chair of Biophysics, and thanks ISF Grant 580/12 for support. We are grateful to the Schmidt Minerva Center on Supramolecular Architecture for its support.

1. Friedl P, Gilmour D (2009) Collective cell migration in morphogenesis, regeneration and cancer. *Nat Rev Mol Cell Biol* 10(7):445–457.
2. Nnetu KD, Knorr M, Strehle D, Zink M, Käs JA (2012) Directed persistent motion maintains sheet integrity during multi-cellular spreading and migration. *Soft Matter* 8(26):2913–2921.
3. Petitjean L, et al. (2010) Velocity fields in a collectively migrating epithelium. *Biophys J* 98(9):1790–1800.
4. Ilina O, Friedl P (2009) Mechanisms of collective cell migration at a glance. *J Cell Sci* 122(Pt 18):3203–3208.
5. Vicsek T, Czirók A, Ben-Jacob E, Cohen I, Shochet O (1995) Novel type of phase transition in a system of self-driven particles. *Phys Rev Lett* 75(6):1226–1229.
6. Szabó B, et al. (2006) Phase transition in the collective migration of tissue cells: Experiment and model. *Phys Rev E Stat Nonlin Soft Matter Phys* 74(6 Pt 1):061908.
7. Henkes S, Fily Y, Marchetti MC (2011) Active jamming: Self-propelled soft particles at high density. *Phys Rev E Stat Nonlin Soft Matter Phys* 84(4 Pt 1):040301.
8. Sepúlveda N, et al. (2013) Collective cell motion in an epithelial sheet can be quantitatively described by a stochastic interacting particle model. *PLOS Comput Biol* 9(3):e1002944.
9. Basan M, Elgeti J, Hannezo E, Rappel W-J, Levine H (2013) Alignment of cellular motility forces with tissue flow as a mechanism for efficient wound healing. *Proc Natl Acad Sci USA* 110(7):2452–2459.
10. Abercrombie M, Heaysman JEM (1953) Observations on the social behaviour of cells in tissue culture. I. Speed of movement of chick heart fibroblasts in relation to their mutual contacts. *Exp Cell Res* 5(1):111–131.
11. Stoker MGP, Rubin H (1967) Density dependent inhibition of cell growth in culture. *Nature* 215(5097):171–172.
12. Angelini TE, et al. (2011) Glass-like dynamics of collective cell migration. *Proc Natl Acad Sci USA* 108(12):4714–4719.
13. Nnetu KD, Knorr M, Käs JA, Zink M (2012) The impact of jamming on boundaries of collectively moving weak-interacting cells. *New J Phys* 14:115012.
14. Yang X, Manning ML, Marchetti MC (2014) Aggregation and segregation of confined active particles. *Soft Matter* 10(34):6477–6484.
15. Bi D, Lopez JH, Schwarz JM, Manning ML (2015) A density-independent rigidity transition in biological tissues. *Nat Phys*, 10.1038/nphys3471.
16. Berthier L, et al. (2005) Direct experimental evidence of a growing length scale accompanying the glass transition. *Science* 310(5755):1797–1800.
17. Cates M, Wittmer J, Bouchaud J-P, Claudin P (1998) Jamming, force chains, and fragile matter. *Phys Rev Lett* 81(9):1841–1844.
18. Liu AJ, Nagel SR (1998) Jamming is not just cool any more. *Nature* 396(6706):21–22.
19. Silbert LE, Ertaş D, Grest GS, Halsey TC, Levine D (2002) Analogies between granular jamming and the liquid-glass transition. *Phys Rev E Stat Nonlin Soft Matter Phys* 65(5 Pt 1):051307.
20. Duclos G, Garcia S, Yevick HG, Silberzan P (2014) Perfect nematic order in confined monolayers of spindle-shaped cells. *Soft Matter* 10(14):2346–2353.
21. Zehnder SM, Suaris M, Bellaire MM, Angelini TE (2015) Cell volume fluctuations in MDCK monolayers. *Biophys J* 108(2):247–250.
22. Sadati M, Taheri Qazvini N, Krishnan R, Park CY, Fredberg JJ (2013) Collective migration and cell jamming. *Differentiation* 86(3):121–125.
23. Sadati M, Nourhani A, Fredberg JJ, Taheri Qazvini N (2014) Glass-like dynamics in the cell and in cellular collectives. *Wiley Interdiscip Rev Syst Biol Med* 6(2):137–149.
24. Fredberg JJ (2014) Power steering, power brakes, and jamming: evolution of collective cell-cell interactions. *Physiology (Bethesda)* 29(4):218–219.
25. Li B, Sun SX (2014) Coherent motions in confluent cell monolayer sheets. *Biophys J* 107(7):1532–1541.
26. Marel A-K, et al. (2014) Flow and diffusion in channel-guided cell migration. *Biophys J* 107(5):1054–1064.
27. Doxzen K, et al. (2013) Guidance of collective cell migration by substrate geometry. *Integr Biol (Camb)* 5(8):1026–1035.
28. Schötz E-M, Lanio M, Talbot JA, Manning ML (2013) Glassy dynamics in three-dimensional embryonic tissues. *J R Soc Interface* 10(89):20130726.
29. Ramirez RD, et al. (2004) Immortalization of human bronchial epithelial cells in the absence of viral oncoproteins. *Cancer Res* 64(24):9027–9034.
30. Marchetti MC, et al. (2013) Hydrodynamics of soft active matter. *Rev Mod Phys* 85(3):1143–1189.
31. Malet-Engra G, et al. (2015) Collective cell motility promotes chemotactic prowess and resistance to chemorepulsion. *Curr Biol* 25(2):242–250.
32. Chang SS, Guo WH, Kim Y, Wang YL (2013) Guidance of cell migration by substrate dimension. *Biophys J* 104(2):313–321.
33. Rolli CG, et al. (2012) Switchable adhesive substrates: Revealing geometry dependence in collective cell behavior. *Biomaterials* 33(8):2409–2418.
34. Humphries JD, et al. (2007) Vinculin controls focal adhesion formation by direct interactions with talin and actin. *J Cell Biol* 179(5):1043–1057.
35. Carisey A, et al. (2013) Vinculin regulates the recruitment and release of core focal adhesion proteins in a force-dependent manner. *Curr Biol* 23(4):271–281.
36. Berthier L, Biroli G, Bouchaud J-P, Cipelletti L, van Saarloos W (2011) *Dynamical Heterogeneities in Glasses, Colloids, and Granular Media* (Oxford Univ Press, Oxford, UK).
37. Steinberg MS, Garrod DR (1975) Observations on the sorting-out of embryonic cells in monolayer culture. *J Cell Sci* 18(3):385–403.
38. Garrahan JP (2011) Dynamic heterogeneity comes to life. *Proc Natl Acad Sci USA* 108(12):4701–4702.
39. Park JA, et al. (2015) Unjamming and cell shape in the asthmatic airway epithelium. *Nat Mater* 14(10):1040–1048.
40. Raffel M, Willert CE, Kompenhans J (1998) *Particle Image Velocimetry. A Practical Guide* (Springer, Berlin).
41. Deforet M, et al. (2012) Automated velocity mapping of migrating cell populations (AVeMap). *Nat Methods* 9(11):1081–1083.
42. Schindelin J, et al. (2012) Fiji: An open-source platform for biological-image analysis. *Nat Methods* 9(7):676–682.
43. Rasband WS (2012) *ImageJ v1.46b* (US Natl Inst Health, Bethesda, MD).
44. Espanol P, Warren P (1995) Statistical mechanics of dissipative particle dynamics. *Europhys Lett* 30(4):191.
45. Basan M, Prost J, Joanny J-F, Elgeti J (2011) Dissipative particle dynamics simulations for biological tissues: Rheology and competition. *Phys Biol* 8(2):026014.
46. Ben-Isaac E, et al. (2011) Effective temperature of red-blood-cell membrane fluctuations. *Phys Rev Lett* 106(23):238103.
47. Marel A, Podewitz N, Zorn M, Rädler JO, Elgeti J (2014) Alignment of cell division axes in directed epithelial cell migration. *New J Phys* 16:115005.
48. Nikunen P, Karttunen M, Vattulainen I (2003) How would you integrate the equations of motion in dissipative particle dynamics simulations? *Comput Phys Commun* 153(3):407–423.
49. Szabó A, et al. (2010) Collective cell motion in endothelial monolayers. *Phys Biol* 7(4):046007.